Remote Sensing of Environment 247 (2020) 111889

Contents lists available at ScienceDirect

Remote Sensing of Environment

journal homepage: www.elsevier.com/locate/rse

Seasonal distributions of ocean particulate optical properties from spaceborne lidar measurements in Mediterranean and Black sea

Davide Dionisi*, Vittorio Ernesto Brando, Gianluca Volpe, Simone Colella, Rosalia Santoleri

Institute of Marine Sciences (ISMAR), Italian National Research Council (CNR), Rome - Tor Vergata, Italy

A B S T R A C T

Assessing the oceanic surface layer's optical properties through CALIOP has been one of the reasons of the extension of the CALIOP mission for 3 more years (2018–2020). This is the first work evaluating the potential use of CALIOP for ocean applications at regional scale in mid-latitude regions (i.e. Mediterranean, MED, and Black Sea, BS) and investigating the added information on ocean particles given by the column integrated depolarization ratio (δ_T) parameter. We implemented and refined a retrieval procedure to estimate this parameter at 1/4 degree of spatial resolution, comparing 7 years of CALIOP observations (2011–2017) to the corresponding Copernicus multi-sensor L3 ocean colour products of the surface particle backscattering coefficient (b_{bp}) and chlorophyll-a concentration (Chl-a). This study pointed out that the current CALIOP sampling is inadequate to detect subtle day-night difference due to plankton diel variability for these basins. At a basin scale, δ_T covaries with b_{bp} for $b_{bp} \geq 0.0015\ m^{-1}$. This is more evident for BS ($R = 0.84$) than for MED ($R = 0.61$). The analysis of seasonal distributions confirm this result for BS, where δ_T has a semi-annual cycle in very good agreement with b_{bp}. In the MED, characterized by different trophic regimes, δ_T shows also some similarities with Chl-a annual cycle. The combined characterization in the MED bioregions of the annual patterns of b_{bp}:Chl-a, δ_T:Chl-a and δ_T:b_{bp} ratios suggested that δ_T parameter can provide valuable information about the non-sphericity and the size of ocean particles.

1. Introduction

Since the quantitative estimates of the downwelling irradiance attenuation coefficient and Chlorophyll-a concentration (K_D and Chl-a, respectively) provided by the Coastal Zone Colour Scanner (CZCS, 1978–1986), ocean colour observations from passive remote sensing satellites changed the comprehension of the upper ocean biogeochemistry of the global ocean as well as the regional basins (McClain, 2009; Blondeau-Patissier, 2014; Brewin et al., 2017; Jackson et al., 2017). Recent improvements both in optical sensors, implemented on in situ and remote-sensing platforms, and in bio-optical algorithms allowed the study of oceanic variables and processes over a wide range of temporal and spatial scales (Brando et al., 2015; Organelli et al., 2017; Sathyendranath et al., 2019).

Within this frame, Lidar (LIght Detection And Ranging) active remote sensing technique constitutes a highly reliable tool for the investigation of the marine environment. This technique provides measurements of several optical and physical parameters of seawater with a resolution and accuracy comparable with that of standard passive remote sensing radiometry (Behrenfeld et al., 2013; Lu et al., 2014). As demonstrated by the continuously growing body of literature, shipborne (Reuter et al., 1995, Barbini et al., 1999, Bukin et al., 2001, Babichenko et al., 2016, Collister et al., 2018) and aircraft lidar (Gordon, 1982, Churnside and Thorne, 2005, Churnside 2014, Schulien et al., 2017, Churnside et al., 2017, Churnside et al., 2018) have been extensively employed in oceanographic studies.

During the last decade, new applications for the plankton retrievals on the global scale were explored with the CALIOP (Cloud-Aerosol Lidar with Orthogonal Polarization) instrument on-board CALIPSO (Cloud-Aerosol Lidar and Infrared Pathfinder Satellite Observation), which gave the glimpse of a '*new lidar era in satellite oceanography*' (Hostetler et al., 2018; Jamet et al., 2019). In fact, though originally designed for retrieving spatial and optical properties of clouds and aerosols, several studies demonstrated that CALIOP can provide valuable information on oceanic optical properties (Behrenfeld et al., 2013, 2017; Churnside et al., 2013; Lu et al., 2014). Furthermore, satellite lidars can be operated under thin clouds, between holes in broken clouds, and in Polar Regions. The first important result was the estimation of the surface particle backscattering coefficient (b_{bp}) at 532 nm combining the column integrated ratio of cross-polarized to co-polarized signal returns (δ_T), K_D values from MODIS (Moderate Resolution Imaging Spectroradiometer) instrument, and a few assumptions supported by empirical evidence (Behrenfeld et al., 2013). Important scientific results were then achieved using CALIOP observations both at global scale and in specific regions: Behrenfeld et al. (2013) and Lu et al. (2014) provided global maps of b_{bp} at the spatial resolution of 2°, phytoplankton carbon biomass and total particulate organic carbon (POC); Behrenfeld et al. (2017) measured the annual cycles of the

* Corresponding author.
E-mail address: davide.dionisi@cnr.it (D. Dionisi).

https://doi.org/10.1016/j.rse.2020.111889
Received 29 November 2019; Received in revised form 5 April 2020; Accepted 11 May 2020

phytoplankton biomass in polar regions. Additionally, the work of Lu et al. (2014) showed that global chlorophyll-a and POC concentrations could be estimated from the values of δ_T, showing a potential new application for CALIOP.

Nonetheless, the vertical resolution of CALIOP prevents to vertically resolve ocean properties and the assumptions made to retrieve satellite b_{bp} largely impact the associated uncertainties. Hence, one of the reasons of the 3 year extension of the CALIPSO mission (2018–2020) is the further assessment of the oceanic surface layer's optical properties through CALIOP (https://directory.eoportal.org/web/eoportal/satellite-missions/c-missions/calipso, last access: 10/03/2020). In fact, the use of CALIOP dataset (and, in perspective, of a future oceanographic lidar satellite) may be especially important to study specific regions and scientific questions such as: the variations in plankton properties under conditions of day and night (diel periodicity, Harding Jr. et al., 1981, 1982); the underestimation of the backscattering models based on Mie theory compared to the measurements of phytoplankton backscattering and of the particulate backscattering in the open ocean (the missing backscattering enigma, Stramski et al., 2004; Organelli et al., 2018).

Within this frame, the objectives of this study are to investigate: a) the potential use of CALIOP for ocean applications in mid-latitude regions such as the Mediterranean (MED) and Black (BS) seas, where the CALIOP ground-tracks are less dense compared to high latitudes due to the polar orbit of CALIPSO; b) the employment of the column integrated depolarization ratio (δ_T) not only to derive lidar b_{bp} but also as a potential ocean colour variable, analyzing the the added information about ocean particles (e.g. size and composition) that this parameter could provide.

To analyze, interpret and reference the CALIOP ocean parameters in the MED and BS, we used the Ocean Colour products provided by the Copernicus Marine Environmental Service (CMEMS). In particular, we compared the CALIOP ocean parameters to the consistently reprocessed multi-sensor L3 time series of b_{bp} at 443 nm and Chl-a over these two regions (Volpe et al., 2019; Kajiyama et al., 2019). We analyzed the annual cycles of b_{bp}, Chl-a and δ_T at basin scale for BS and MED and, for the latter basin only, also at sub-basin scale; we then examined the δ_T:Chl-a, δ_T:b_{bp} and b_{bp}:Chl-a relationships in the MED as a function of seasons and bioregions.

In Section 2 we describe CALIOP and CMEMS data and the adopted and refined procedures to retrieve ocean parameters from CALIOP. Section 3 shows and discusses the results of the comparisons between δ_T and b_{bp} and Chl-a in the considered basins and, finally, Section 4 summarizes the developed approach and the achieved main results and provides recommendations for future oceanographic studies using polarized lidar measurements.

2. Data and methods

In this section, we describe both the main characteristics of the data that were extensively used in this work along with the developed routines that were put in place to process them. The products include the ocean colour multi-sensor CMEMS data and the CALIOP version 4.1. The state-of-the-art CALIOP retrieval procedure is based on the methods developed by Churnside et al. (2013), Behrenfeld et al. (2013) and Lu et al. (2014).

2.1. CMEMS Ocean colour product

As one of the six services of the Copernicus program, CMEMS provides sustained observations of physical and biogeochemical variables for the global ocean and the European seas (Le Traon et al., 2019). For this work, we used, as reference, the CMEMS multi-sensor regional L3 products of b_{bp} at 443 nm and Chl-a in the MED and BS. The multi-sensor time series is retrieved with a processing chain that involves the pre-processing of L2 data from different sensors merged together over a common set of wavelengths (Volpe et al., 2019): the SeaWiFS, MODIS-AQUA and VIIRS L2 data were obtained from NASA-OBPG (R2018.0), while MERIS data are from the ESA third reprocessing with POLYMER atmospheric correction scheme, made available by Plymouth Marine Laboratory in the United Kingdom.

The CMEMS regional Chl-a products blend the appropriate regional algorithms depending on the water types ensuring that the bio-optical characteristics of each regional sea are accounted for during development and data validation (Le Traon et al., 2019; Kajiyama et al., 2019; Volpe et al., 2019). In the Mediterranean Sea, the blended chlorophyll product is based on two algorithms: for open ocean waters the MedOC4, an updated version of the regionally parameterized Maximum Band Ratio (Volpe et al., 2007, 2019), while for the optically complex waters domain the ADOC4 algorithm (D'Alimonte and Zibordi, 2003) is used. For the Black Sea, a merging scheme (Kajiyama et al., 2019) has been designed to use a two band ratio algorithm (510 and 555 nm, Zibordi et al., 2015) for open ocean waters whilst a Multilayer Perceptron (MLP) neural net based on three bands (490, 510 and 555 nm) for the optically complex waters domain. For both basins, b_{bp} at 443 nm is retrieved using the Quasi-Analytical Algorithm (QAA v6, first developed by Lee et al., 2002). All data in the CMEMS catalogue are freely and publicly available at the http://marine.copernicus.eu.

2.2. CALIOP data

The CALIPSO satellite, launched in April 2006, is part of the A-Train satellite constellation, with a sun-synchronous polar orbit at 705 km altitude, 16-day repetition cycle and a nominal ascending node Equator crossing time of 13:30 (01:30) local daytime (night-time) (Liu et al., 2009). The CALIOP instrument is a three-channel elastic backscatter lidar that provides measurements of attenuated backscatter coefficients at 532 nm and at 1064 nm, with an horizontal resolution of 1/3 km and a vertical resolution varying with altitude: 30 m from ground to 8.2 km, 60 m from 8.2 to 20.2 km, and 180 m from 20.2 to 30.1 km (Winker et al., 2009; Huang et al., 2015). Fig. 1 depicts the CALIPSO ground tracks over the Mediterranean and Black seas. At these latitudes, the neighboring ground tracks are approximately spaced 150 km. To highlight the spatial sampling difference between night-time and the corresponding daytime orbit, in Fig. 1 a night-time ground-track N1 (N2) in BS (MED) is labeled with the corresponding daytime ground-track D1 (D2).

CALIOP version 4.1 level 1 (L1) data products were used here to derive the ocean parameters of interest for this study. This data version is characterized by significant upgrades regarding the calibration accuracy and the ancillary data used for the surface detection and calibration with respect to previous versions (Getzewich et al., 2018). In particular, the likelihood of the signal saturation returning from the planetary surface is introduced in the data products (Lu et al., 2018). This information, which is crucial for the retrieval of ocean product (see Section 2.3), is reported as a flag value assuming the integer values of 0, 1 or 2 for a not saturated, possibly saturated or certainly saturated detection channel, respectively. More information about the data products can be found at the Atmospheric Science Data Center (ASDC) web site (https://eosweb.larc.nasa.gov/project/calipso/calipso_table, last access: 10/03/2020).

2.3. CALIOP retrieval procedure for ocean applications

The primary data set includes the vertical profiles of co-polarized and cross-polarized component of the attenuated backscatter coefficients at 532 nm ($ß_{co}$ and $ß_{cr}$, respectively), with a vertical resolution of 30 m (22.5 m, in water) and a single-shot along-track horizontal resolution of 330 m. To deal with data with an accuracy as high as possible, a preliminary filtering procedure is applied to the dataset, according to the following criteria:

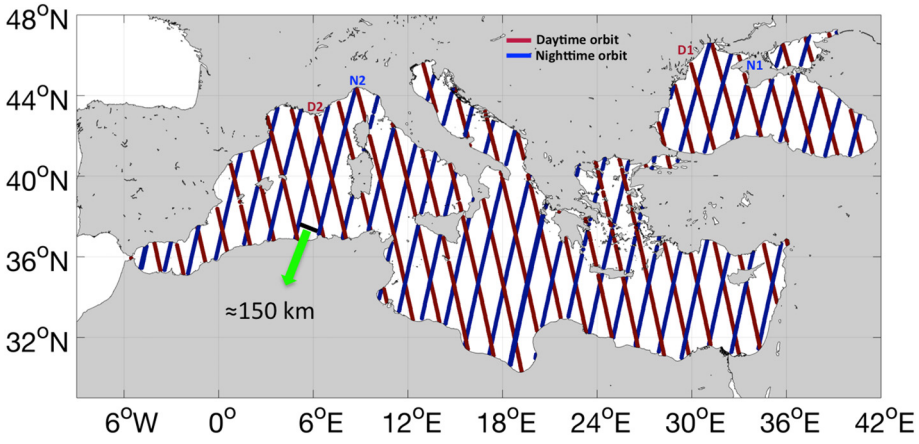

Fig. 1. Geographic distribution of CALIPSO ground tracks over the Mediterranean and Black seas. Red lines represent the ascending CALIOP daytime orbits, and blue lines are the descending night-time orbits. As an example, a night-time orbit in BS (N1) and in MED (N2) are labeled with the corresponding daytime orbits (D1 and D2, respectively). (For interpretation of the references to colour in this figure legend, the reader is referred to the web version of this article.)

1. only profiles with surface peaks (i.e. maximum peaks of the attenuated backscatter) located within ± 120 m (± 4 bins) of the "Surface_Elevation" parameter of the Digital Elevation Model (DEM) recorded in the CALIOP L1 data are considered. This procedure permits to reject the signal peaks caused by low-lying atmospheric layers (Lu et al., 2016). If the peak is not within this range, that profile is not used in the analysis.
2. The surface backscatter signal for both $ß_{co}$ and $ß_{cr}$ must not be saturated (i.e. Surface_Saturation_Flag_532 = 0, Lu et al., 2018).
3. The Integrated Attenuated Backscatter (IAB) must be lower than 0.017 sr^{-1}. This allows selecting only clear sky conditions (Josset et al., 2010b).

This procedure reduces the original data sample of around 67% (from 123 k to 42 k $ß_{co}$ profiles per year) as reported by Table 1, where the impact of each filtering step is resumed in terms of number of $ß_{co}$ profiles per year.

After this preliminary filtering, the CALIOP measurements are averaged into profiles with a horizontal along-track resolution of 10 km, maintaining the 330 m across-track resolution. A similar integration allows increasing the signal-to-noise ratio of the CALIOP profile and, thus, taking into account in the procedure the 3th bin below the surface (~50 m depth, Churnside et al., 2013). The subsurface $ß_{co}$ and $ß_{cr}$ profiles are affected by the strong signal return from the ocean surface because of the transient response of CALIOP photomultiplier tubes (PMT). This signal contamination, due to the PMT's noise tail effect and low-pass filter's broadening effect (Hu et al., 2007; McGill et al., 2007; Lu et al., 2013, 2014), involves several range bins adjacent to the surface bin. These effects have a higher impact on the cross-polarized channel than on the co-polarized channel, providing a depolarization profile (i.e. the ratio between $ß_{cr}$ and $ß_{co}$) with underestimated values (Lu et al., 2014). Consequently, to remove the transient response effect, a de-convolution method (Li et al., 2011; Lu et al., 2014) has been implemented in our analysis. Then, only the corrected attenuated backscatter coefficient profiles ($ß_{co\_corr}$ and $ß_{cr\_corr}$, respectively) that have all the first three bins below the surface with values greater than zero are selected.

Table 1
List of filtering procedure steps and the corresponding number of analyzed CALIOP profiles.

Filtering steps	Number of profiles per year
Starting data (10 km horizontal resolution)	123,000
1) Surface peak signal located within ± 4 bins of the "Surface_Elevation"	105,000
2) Surface_Saturation_Flag_532 = 0	92,000
3) IAB < 0.017 sr^{-1}	45,000
4) First 3 bin values below the surface > 0	25,000
5) $\delta_T \leq 0.5$	21,000
6) 3 m $s^{-1} \leq w <$ 8 m s^{-1}	18,000
(7) gridded bins with z < −70 m	
Final data (0.25° gridded bins)	3150

The corrected profiles, which reduced to about 20% of the original data sample (see Table 1), are used to compute the integrated total (δ_T) and the ocean subsurface depolarization ratio (δ_w), defined with the same notation as Lu et al. (2014):

$$\delta_T = \frac{\sum_{i=p}^{i=p+2} \beta_{cr\_corr}(z_i)}{\sum_{i=p}^{i=p+2} \beta_{co\_corr}(z_i)} \quad (1)$$

$$\delta_w = \frac{\sum_{i=p+1}^{i=p+2} \beta_{\perp}^{corr}(z_i)}{\sum_{i=p+1}^{i=p+2} \beta_{\parallel}^{corr}(z_i)} \quad (2)$$

where p indicates the peak surface return bin.

The CALIOP data with $\delta_T > 0.05$ were removed from our analysis (Lu et al., 2014). The column-integrated ocean subsurface lidar backscatter (γ) is then obtained combining Eqn 1 and Eqn 2:

$$\gamma = \frac{0.0209}{4\pi\sigma^2 cos^4\theta} exp\left[-\frac{tan^2\theta}{2\sigma^2}\right] \frac{\delta_T}{1-\delta_T/\delta_w} \quad (3)$$

where the ocean surface mean squares wave slopes (σ^2) are estimated using wind speed (w) derived by the wind re-analysis of ECMWF atmospheric reanalysis ERA5 (Hersbach, 2016). To ensure consistency with previous works (Behrenfeld et al., 2013; Lu et al., 2014), low and high winds (w < 3 m s^{-1} and w > 8 m s^{-1}, respectively) have been both removed from the analyzed dataset. Finally, to avoid the signal contamination from the sea bottom in the deeper CALIOP bin considered in the analysis, only the sea grid points deeper than 70 m are considered in this study. The associated relative uncertainty ($\Delta\gamma/\gamma$) is 0.15, as estimated by Lu et al. (2014). The results of the implemented procedure, applied to Mediterranean and Black Sea basins, are summarized in Fig. 2. The mean values computed over the period 2011–2017 of Chl-a and b_{bp} (Fig. 2 a and b, respectively) from CMEMS and of δ_T (Fig. 2c) are presented, along the CALIOP ground-tracks with a final horizontal resolution of 0.25°.

The total number of valid values, after the filtering procedure (Table 1), is 22,052 for the period 2011–2017: roughly 3150 values per year. A high correlation (R) is observed between γ and δ_T for both BS ($R = 0.91$, $N = 1893$) and MED ($R = 0.86$, $N = 20{,}159$). This result, which is quite similar to the one estimated at a global scale ($R = 0.96$; Lu et al., 2014), allows using δ_T instead of γ in the comparison between CALIOP and CMEMS data.

The choice of δ_T as the focus parameter for this study has the advantage to use a parameter with a lower associated uncertainty, being estimated only through lidar measurements without using any

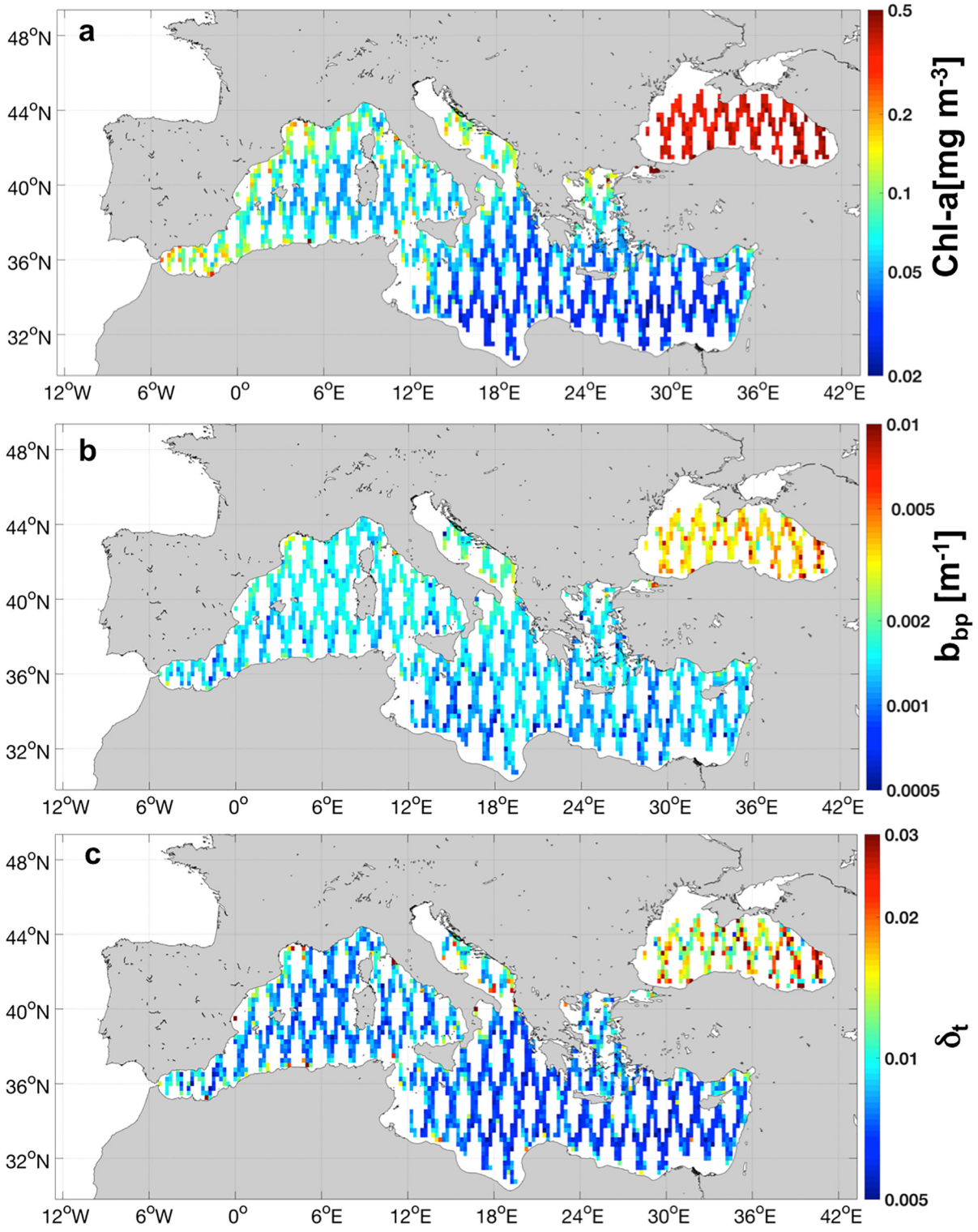

Fig. 2. Distribution of Chl-a, b_{bp} and δ_T median values over the period 2011–2017 along the CALIOP ground-tracks (a, b, c, respectively) obtained from CMEMS products (a and b) and from Eq. (1) for δ_T (c). The horizontal resolution of the gridded bins is 0.25°. Only grid points with sea depth > 70 m are depicted.

assumptions and ancillary measurements as in the case of b_{bp} (Behrenfeld et al., 2013). The depolarization ratio parameter has been extensively studied for atmospheric applications (Cai and Liou, 1982; Takano and Liou, 1989; Yang and Liou, 1996) but only few works used it over the ocean (Churnside, 2008; Josset et al., 2010a; Churnside, 2014; Qun et al., 2019). Thus, the drawback is that the information about the oceanic optical properties carried by the interaction of polarized lidar signal with particles in seawater has not been unequivocally determined and characterized so far. It has to be noted that absorption processes do not directly affect δ_T; this is given by the fact that the cross- and co-polarized signals do result from elastic scattering processes between emitted polarized radiation and particles.

3. Results and discussions

To study the relationships between δ_T and b_{bp} and Chl-a, these

variables are compared both at basin scale (Section 3.2) and, for the Mediterranean, at sub-basin scale (Section 3.3). Section 3.4 presents the behavior of δ_T:Chl-a and δ_T:b_{bp} ratios compared to b_{bp}:Chl-a ratio, as a function of seasons and distinct bioregions. Next section deals with the issues and the implications linked to the CALIOP sampling strategy (both day and night) and of the standard ocean colour radiometry (daytime only).

3.1. Day and night data sampling

CMEMS data include only daytime measurements, whereas CALIOP acquires data during both night and day. In this study, we used both CALIOP daytime (ascending orbit) and night-time (descending orbit) ground-tracks (see Fig. 1) and the corresponding spatial collocated CMEMS gridded bins. In the case of the daytime acquisitions, the absolute temporal difference ($|\Delta t|$) between each bin of CALIOP and CMEMS product is ≤ 6 h, while it is around 12 h in the case of the night-time acquisitions.

Recently, the exploitation of daytime and night-time CALIOP dataset allowed observing the daily vertical migrations of ocean animals (Behrenfeld et al., 2019). However, over the entire Mediterranean or Black sea and with the spatial resolution of 0.25°, the two CALIOP orbits (day and night) cover different bioregions and water types, making such observations difficult or at least not necessarily linked to the animals diel vertical migration. To verify the impact of the CALIOP sampling strategy on the uniformity of the spatial sampling, we calculated the annual cycles of the Chl-a and b_{bp} in MED and BS for the CMEMS datasets that corresponds to the two types of CALIOP ground-tracks for the period 2011–2017 (N_{day} = 10,294, N_{night} = 9865 for MED and N_{day} = 943, N_{night} = 950 for BS). This comparison, depicted in Fig. 3, highlights that the Chl-a and b_{bp} annual cycles are characterized by a large variability in terms of interquartile range. Furthermore, the non-overlapping of the two annual cycles of b_{bp} and, in part, of Chl-a attests that CALIOP daytime and night-time ground-tracks observe different water types. Hence, this analysis suggests that, contrarily to open ocean areas, at basin scale, CALIOP temporal and spatial sampling drive the Chl-a and b_{bp} variability for the ascending and descending orbits. This is due to the different bio-optical and trophic regimes of the considered basins. For these reasons, in Mediterranean and Black Sea, CALIOP observations are not able to detect subtle day-night difference associated with plankton optical properties.

3.2. Basin scale analysis

Fig. 4 presents the density plots of δ_T against b_{bp} and Chl-a for the two basins. It has to be noted that Fig. 4 is presented in log-log scale only to improve the readability of the data, but that all the correlation coefficients and the linear fits reported in this work have been calculated using non-transformed data. Regarding δ_T vs b_{bp}, moderate (R = 0.61) and high correlation (R = 0.84) are observed for MED and BS (Fig. 4a and b, respectively). Conversely, δ_T and Chl-a are poorly (R = 0.42) and no correlated at all (R = 0.01) in the two basins (Fig. 4c and d, respectively). For significant R values ($R > 0.6$), the slope of the linear relationship between δ_T and b_{bp} is equal to 4.77 (BS) and 5.06 (MED). The observed differences between δ_T vs Chl-a and the δ_T vs b_{bp} reflect the different trophic regimes and optical conditions characterizing the two basins. For productive or optically complex waters with values of $b_{bp} > 0.0015$ m^{-1}, dominated by coastal trophic regime and river runoffs, as the BS (Ludwig et al., 2009), δ_T agrees very well with the b_{bp}. This confirms the findings of Collister et al. (2018), which observed that the linear depolarization ratio measured by a shipboard lidar well agrees with in situ measurements of the particulate backscattering ratio (b_{bp}/b_p). The correlation between δ_T and b_{bp} can be explained, at the first order, by the fact that the cross-polarization signal received by CALIOP is almost entirely due to the backscatter from ocean particulate matter, as the contribution in signal polarization

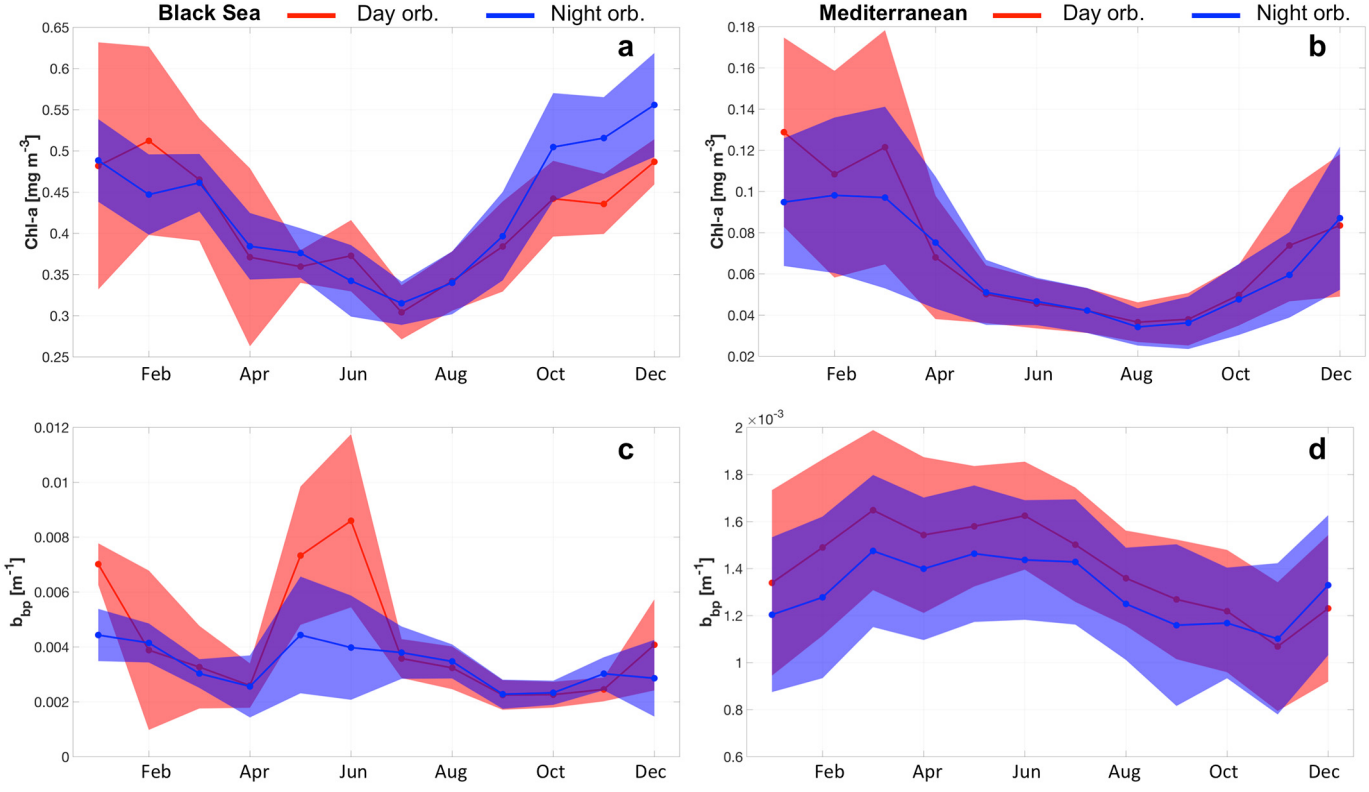

Fig. 3. Annual cycles of the Chl-a (a and b panels) and b_{bp} (c and d panels) in terms of medians (solid lines) and the interquartile ranges (colored areas) for the day and night CALIOP ground tracks (red and blue, respectively) in the Black sea (left column) and in the Mediterranean Sea (right column). Note that each panel has its own optimized y-axis scale. (For interpretation of the references to colour in this figure legend, the reader is referred to the web version of this article.)

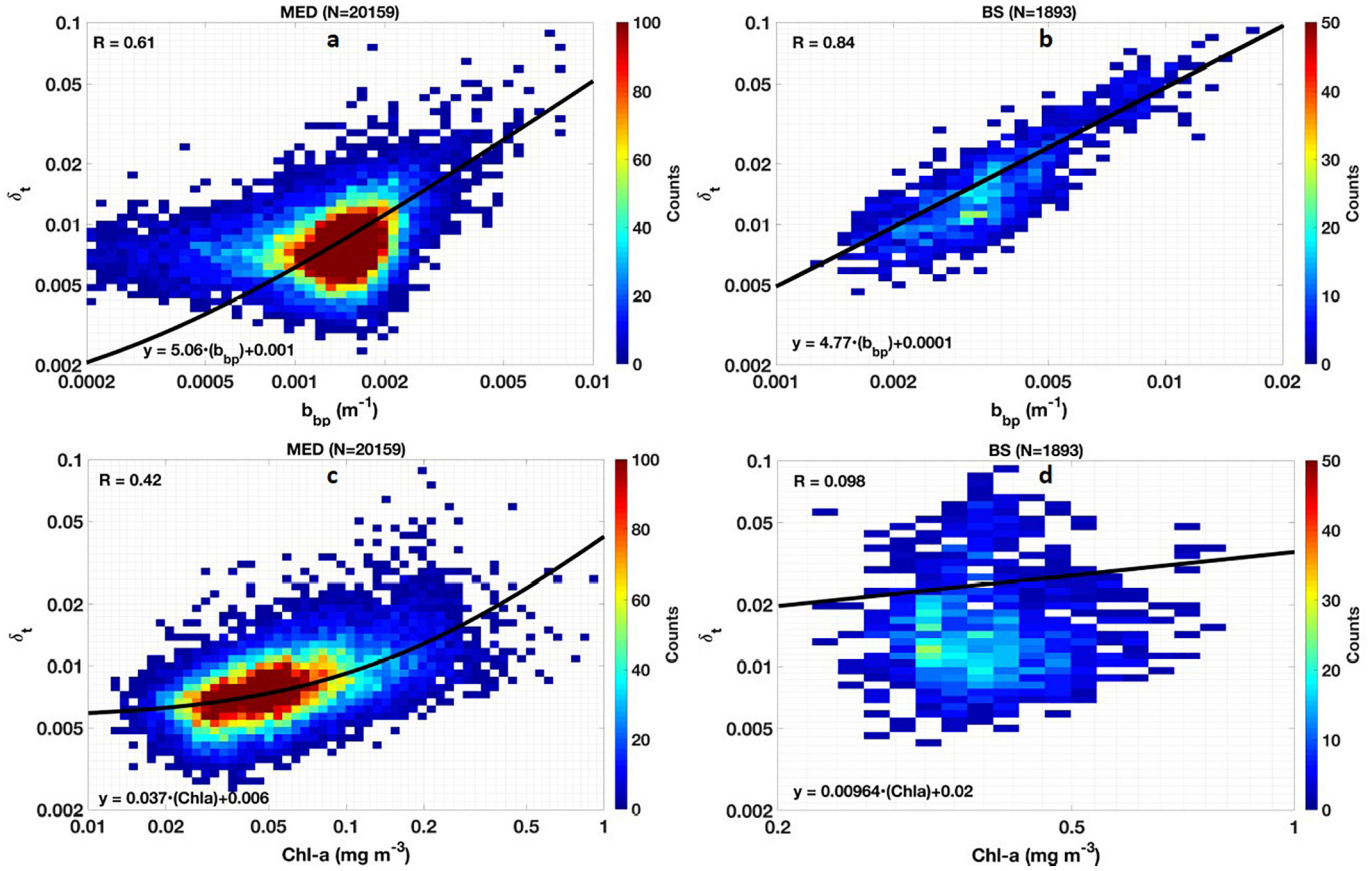

Fig. 4. Log-log density plot of the integrated total depolarization ratio (δ_T) as a function of b_{bp} at 532 nm (plot a and c, respectively) and of the Chl-a (plot b and plot d, respectively) for Mediterranean and Black Sea. The colour code indicates the number of the analyzed values. The black lines represent the results of the linear fit between the considered parameters.

by either surface Fresnel reflection or water molecules can be negligible (Churnside, 2008; Behrenfeld et al., 2013).

The different trophic conditions of the MED, where Chl-a and b_{bp} vary over 1 order of magnitude, prevent to observe a clear relationship between the variables. However, also in this basin, for b_{bp} values $>$ 0.0015 m^{-1}, δ_T seems to correlate with b_{bp}, whereas for values lower than 0.0008 m^{-1} δ_T seems to reach a detection limit (see Fig. 4a).

The highlighted differences of the two basins in terms of trophic regimes and optical conditions clearly arise from Fig. 5, where the annual cycles of Chl-a, b_{bp} and δ_T have been computed on a monthly basis in terms of medians and associated interquartile ranges. For the Black Sea, δ_T has a semi-annual cycle that is in very good agreement with b_{bp} with two maxima around May/June and December/January and two minima in September and March. For the Mediterranean, δ_T has an annual cycle characterized by a summertime minimum and a winter early spring maximum that has some analogies with Chl-a cycle but has also some similarity with the b_{bp} cycle. Thus, one result emerging from Figs. 4 and 5 is a sort of '*dual*' behavior of δ_T parameter: in the Black Sea, which is characterized by the presence of productive or optically complex waters, δ_T is closely related to b_{bp} patterns; in the Mediterranean, where different trophic conditions are present, δ_T shows also some similarities with Chl-a annual cycle. It is important to recall that, as specified in Section 2.3, the δ_T parameter is derived using the first 3 bins below the sea surface. However, recent works (Behrenfeld et al., 2017, 2019) used the first bin only below surface. Here, to assess whether the above results depend somehow on the number of bins used, a sensitivity analysis was performed comparing δ_T computed with 1 and 3 bins, respectively. The result of this analysis (not shown) attests that the use of 1 or 3 bins produces negligible differences both at basin scale, in both basins (MED and BS) and at sub-basin scale (i.e. in the Mediterranean bioregions considered in Section 3.3).

3.3. Sub-basin scale analysis

The Mediterranean Sea can be divided in several bioregions corresponding to different bio-optical and trophic regimes (D'Ortenzio and Ribera d'Alcalà, 2009, Bellacicco et al., 2016, Basterretxea et al., 2018). Fig. 6 presents the bioregions used in this work to explore the relationships between Chl-a, b_{bp} and δ_T: NorthWest (NW), SouthWest (SW), Tyrrhenian (TY), Ionian (IO), Levantine (LV). Due to the low number of CALIOP ground-tracks with sea-bottom deeper than 70 m (see Fig. 2) in the Adriatic sea (AD), this region has been excluded from the analysis.

Tables 2 and 3 report the seasonal correlation coefficient of δ_T with Chl-a and b_{bp} for the Mediterranean bioregions. As for the analysis at basin scale (see Section 3.2), no significant correlation is observed between Chl-a and δ_T, except for the spring in the Tyrrhenian Sea (Table 2). Conversely, the results of Table 3 suggest that δ_T covaries with b_{bp}, depending on the season and on the bioregion. In particular, a significant and systematic correlation is found during spring and winter for the western regions (NW and SW) and TY. This is not observed for the oligotrophic sub-basins (IO and LV) excepting for the winter in LV.

To better comprehend these results, the annual cycles of Chl-a, b_{bp} and δ_T are depicted in Fig. 7 for each bioregion. NW, SW and TY sub-basins have similar patterns in terms of b_{bp} and δ_T, with highest values during February/March and minimal values for August/September. Overall, the significant values of R (Table 3) in correspondence of winter and spring in the NW, SW and TY are likely due to the high bbp values (i.e. b_{bp} $>$ 0.0015 m-1) reached in February (for winter) and

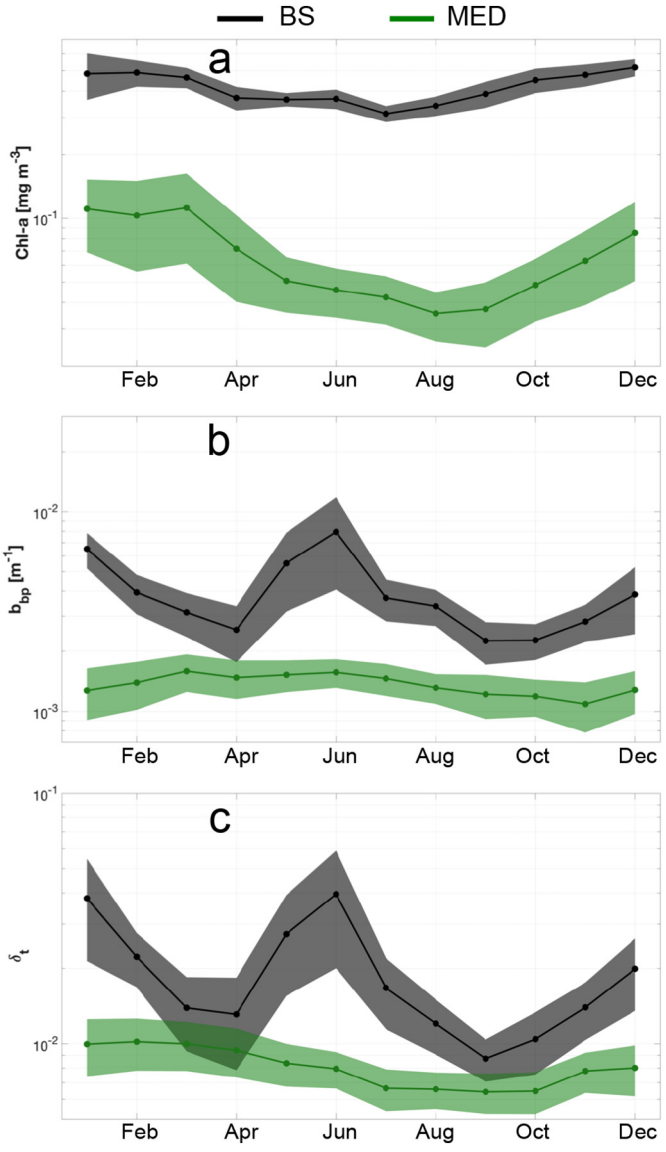

Fig. 5. Annual cycles of Chl-a, b_{bp} and δ_T (a, b and c panel, respectively) in terms of medians (black lines) and the interquartile ranges (colored areas) for the Black Sea and Mediterranean (black and green colors, respectively). (For interpretation of the references to colour in this figure legend, the reader is referred to the web version of this article.)

Table 2
Seasonal correlation coefficients (R) between Chl-a and δT for the Mediterranean bioregions (DJF = December January February; MAM = March April May; JJA = June July August; SON = September October November). In parenthesis the number of samples. Significant R values ($R \geq 0.6$) are highlighted in bold. Values are computed without transforming data into their logarithm.

	NW	SW	TY	IO	LV
DJF	0.54(240)	0.52(419)	0.57(196)	0.32(787)	0.43(895)
MAM	0.29(440)	0.50(774)	**0.79**(377)	0.23(1380)	0.48(1383)
JJA	0.32(773)	0.33(1454)	0.44(554)	0.16(2309)	0.41(2645)
SON	0.47(407)	0.33(757)	0.36(253)	0.21(1869)	0.53(1531)

Table 3
Seasonal correlation coefficients between bbp and δT for the five Mediterranean bioregions. In parenthesis the number of samples used for each R. Significant R values ($R \geq 0.6$) are highlighted in bold and the number of samples used for each R is indicated in parenthesis.

	NW	SW	TY	IO	LV
DJF	**0.67** (240)	**0.70** (419)	**0.83** (196)	0.37 (787)	**0.67** (895)
MAM	**0.67** (440)	**0.60** (774)	**0.84** (377)	0.42 (1380)	0.56 (1383)
JJA	0.32 (773)	0.21 (1454)	0.26 (554)	0.16 (2309)	0.28 (2645)
SON	0.42 (407)	0.43 (757)	0.21 (253)	0.15 (1869)	0.44 (1531)

March (for spring), thus affecting the computation. On the contrary, the relationship between b_{bp} and δ_T is not observed with low b_{bp} values (i.e. in summer and autumn, and in the oligotrophic sub-basins).

In terms of Chl-a, west MED sub-basins (NW and SW) and TY have an annual cycle similar to b_{bp} and δ_T with the exceptions of the March NW bloom peak and an autumnal increasing trend that is not so visible in the other variables. This can be interpreted as a sign of photo-acclimation, for which phytoplankton cells increase their chlorophyll content to better capture light given the seasonal availability of new nutrients. For the eastern oligotrophic sub-basins, although the point-by-point correlation is not significant, the annual cycles of Chl-a and δ_T are quite similar with summertime minima and wintertime maxima in opposition to the b_{bp} that seems to be in anti-phase with the highest values in June and lowest values in November. The low Chl-a signal associated with the high scattering is an indication of the presence of non-pigmented particles that populate the upper ocean: low nutrient low chlorophyll regions are associated with an increased concentration of small heterotrophs like bacteria in relation to phytoplankton concentration, with strong implication for the entire food web (Cho and Azam, 1990; Gasol et al., 1997).

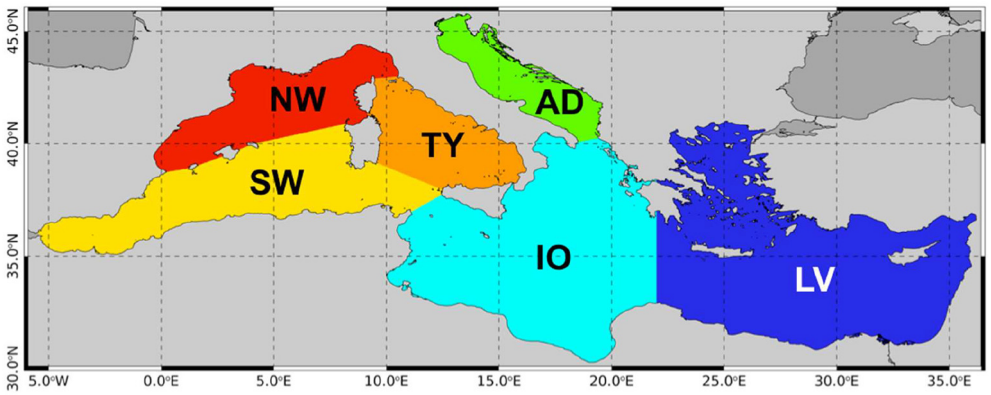

Fig. 6. Map of the Mediterranean bioregions: NorthWest (NW), SouthWest (SW), Tyrrhenian (TY), Ionian (IO), Levantine (LV), Adriatic (AD).

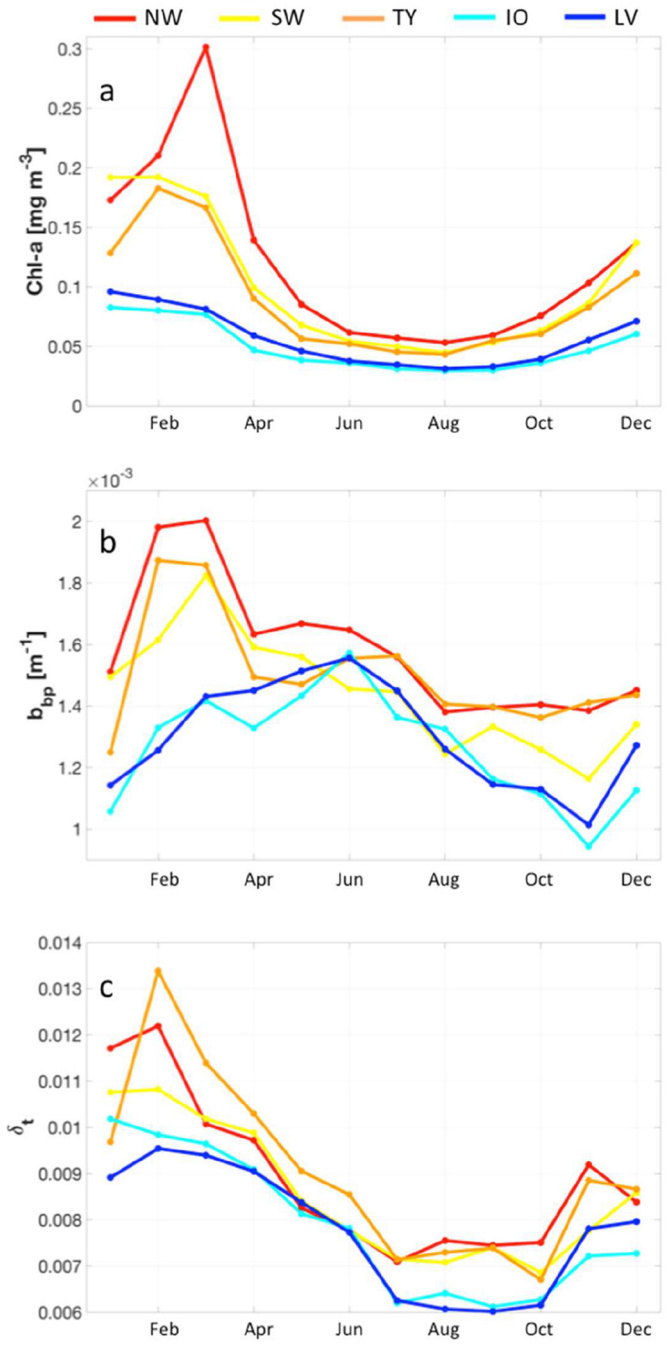

Fig. 7. Median annual cycles of Chl-a, b_{bp} and δ_T (a, b and c panel, respectively) for the five Mediterranean bioregions of Fig. 6.

3.4. b_{bp}:Chl-a, δ_T:b_{bp} and δ_T:Chl-a ratio analyses

The b_{bp} and Chl-a variables are generally employed as indicators of POC and phytoplankton carbon biomass concentrations, respectively (Cullen, 1982; Stramski et al., 1999; Balch et al., 2001; Cetinić et al., 2012; Siegel et al., 2013; Dall'Olmo and Mork, 2014). It is known however that the chlorophyll concentration variability may also reflect changes in phytoplankton physiological states. In other words, phytoplankton cells must synthesize chlorophyll to capture light for photosynthesis in quantity which are inversely proportional to the amount of ambient light and directly proportional to the availability of nutrients: this seasonally translates, at the latitudes of the Mediterranean and Black seas, into high chlorophyll concentration in winter (low light, high nutrients) and low at summertime (Bellacicco et al., 2016). This process is independent on the number of cell divisions, which are associated with phytoplankton growth (Behrenfeld et al., 2008).

Over wide chlorophyll gradients, b_{bp} and Chl-a exhibit high covariability (Barbieux et al., 2018). However, the relation between Chl-a and b_{bp} is mostly driven by the trophic regime of the region (i.e., the bioregions): high positive correlation is obtained in correspondence of regions populated by pigmented particles (phytoplankton), high negative temporal correlation characterizes regions with a dominance of seasonal alternation of pigmented and non-pigmented particle. No or poor correlation is of areas more or less constantly dominated by non-algal particles (NAPs, Barbieux et al., 2018, Xing et al., 2019). With the aim of investigating the potential added value that could be provided by δ_T, the annual cycles of the b_{bp}:Chl-a, δ_T:Chl-a and δ_T:b_{bp} ratios are depicted in Fig. 8 for the Mediterranean bioregions.

The observed relationship of b_{bp}:Chl-a ratio (Fig. 8a–e) for the considered CMEMS dataset are similar to the results found by Barbieux et al. (2018) that used biogeochemical-Argo floats. A west-to-east trophic gradient characterizes this ratio: NW and SW have similar patterns, lower values for both the ratio and the variability range (0.008 and 0.008–0.03 mg^{-1} m^{-2}, respectively); conversely, the oligotrophic regions (IO and LV) have the highest values of the ratio (0.044 mg^{-1} m^{-2}) and of the variability range (0.012–0.044 mg^{-1} m^{-2}); TY region seems to be in between these two bioregions.

The δ_T:Chl-a ratio (Fig. 8f–j) pattern is very similar to that shown by b_{bp}:Chl-a ratio, confirming the observed correlation between δ_T and b_{bp} (see Sections 3.2 and 3.3): the b_{bp}:Chl-a patterns for NW and SW are well reproduced by the δ_T:Chl-a (including the March bloom minimum of NW); IO and LV bioregions have the highest values of the ratio but a lower variability range compared to b_{bp}:Chl-a (see Section 3.3); the observed pattern for TY region is similar to those of the west regions.

The analysis of the δ_T:b_{bp} annual cycle (Fig. 8k–o) points out some interesting features: the highest (lowest) values of the ratio are measured on January (July) for all the bioregions; the eastern sub-basins (IO and LV) have a marked decreasing (increasing) trend from January to July (from July to November); the western sub-basins (NW, SW and TY) are characterized by less pronounced decreasing trends with different secondary maxima/minima.

The work of Sassen (1991) found that the depolarization ratio values are mainly dependent on particle shape. Hence, at a first order, the observed lowering of the δ_T:b_{bp} ratio could be related to the increase of particle with spherical shape, which, in turn, could be associated with the increase of small particles with a near-spherical shape. The values of the b_{bp}:Chl-a ratio has been recently attributed to changes in the phytoplankton community composition (Cetinic et al., 2012). The coupled analysis of δ_T:b_{bp} and b_{bp}:Chl-a ratios could help in deriving information about these changes. For example, in west MED bioregions (NW and SW), several works (Marty and Chiaverini, 2010; Mayot et al., 2016; Siokou-Frangou et al., 2010) explained the low b_{bp}:Chl-a values as due to the predominance of micro-phytoplankton during the spring bloom, and high b_{bp}:Chl-a values in summer as being mostly due to the dominant contributions of pico- and nano-phytoplankton to the total chlorophyll biomass (Barbieux et al., 2018) and by the increase of NAPs (Sammartino et al., 2015). Thus, the observed decrease of δ_T:b_{bp} values from spring to summer could be related to changes in the phytoplankton community composition, which impacts the non-sphericity and the size of the particles. This decrease is more evident in oligotrophic regions (IO and LV), where high values of b_{bp}:Chl-a are normally associated with the photoacclimation of phytoplankton cells to high light low nutrient conditions (Bellacicco et al., 2016).

These results seems to be confirmed also by looking at the maps of the Phytoplankton Size Classes (PSCs) estimated by the regional PSC algorithm developed by Di Cicco et al. (2017). In particular, an increase of the relative contributions of pico- and nano-phytoplankton to the total Chl-a concentration is observed during summer over the

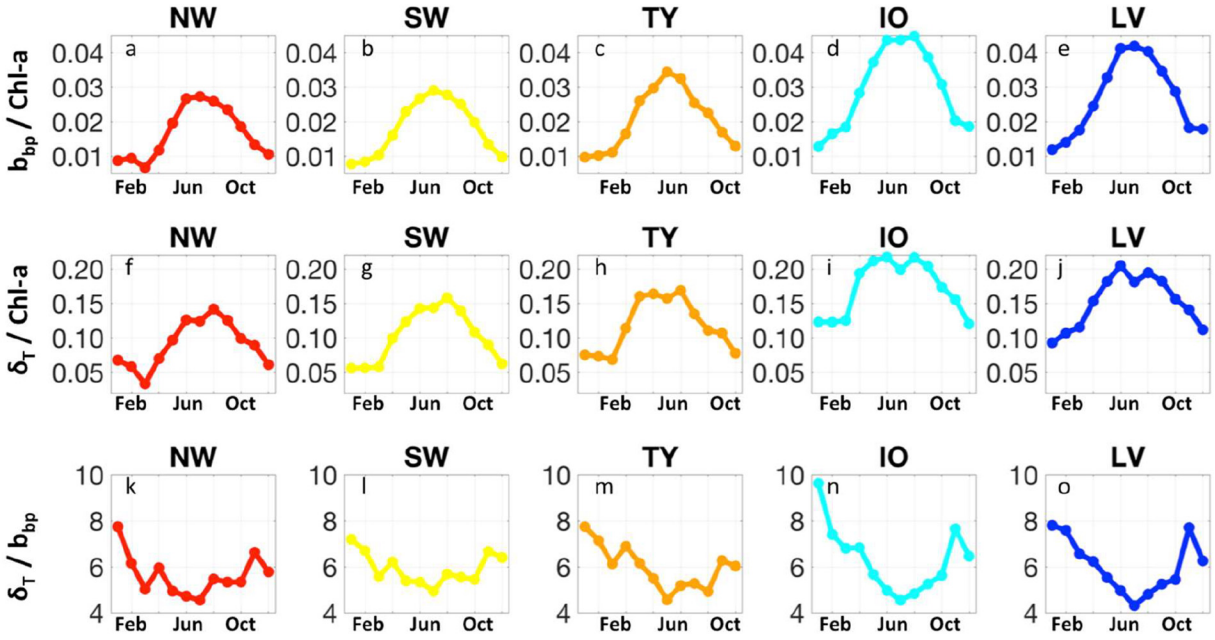

Fig. 8. Annual cycles of the b_{bp}:Chl-a, δ_T:Chl-a and δ_T:b_{bp} ratios for the Mediterranean bioregions defined in Fig. 6 (high, middle and low panel, respectively).

Mediterranean Sea (see Fig. 7a of Di Cicco et al., 2017). However, to better relate the particle parameters (e.g. size, non-sphericity, etc.…) to the observed seasonal trends of δ_T:b_{bp}, we need to consider the PSC variation in terms of particle density (number of particles per unit volume) and particle volume concentration (total particle volume per unit volume). This has been done in the work of Di Cicco (2014), where, following the approach of Kostadinov et al. (2009), the seasonal variability of the PSC was computed for different MED bioregions. This study highlighted that the predominance, in density and volume, of the pico component with respect to the other components increased during summer, particularly in IO and LV sub-basins. These results are in agreement with our assumptions that the changes in the phytoplankton community could be reflected in the observed trend of δ_T:b_{bp} values.

These hypotheses need to be explored with further studies, as the relationship between the Lidar depolarization ratio and the size parameter (i.e. the product of 2π and radius of the scattering sphere divided by the wavelength of the incident radiation) is not systematic, depending on particle shape and refractive index (Mishchenko and Hovenier, 1995; Sassen, 2005). Additionally, before using the information contained in the depolarization signal, it is necessary to evaluate the contribution of multiple scattering (Bissonnette, 2005), which depends on several factors. In particular, a recent work of Qun et al. (2019) showed that *large field-of-view, a high single scattering albedo and large beam attenuation coefficient enhance the multiple scattering effect between photons and particles*. The impact of these factors on the original value of δ_T still needs to be quantitatively assessed.

4. Summary and conclusions

The main objective of the present work was to evaluate the ocean application of CALIOP observations at mid-latitude regions (i.e. Mediterranean and Black Sea). Based on the works of Churnside et al. (2013), Behrenfeld et al. (2013) and Lu et al. (2014), a retrieval algorithm using the first three lidar bins below the ocean surface was implemented and refined to estimate the CALIOP ocean parameters such as the integrated total depolarization ratio (δ_T) and the column-integrated ocean subsurface lidar backscatter (γ) at a horizontal spatial resolution of 0.25°. These parameters were computed for 7 years of CALIOP dataset (2011–2017) and compared to the CMEMS multi-sensor L3 products of b_{bp} at 443 nm and Chl-a.

Regarding the CALIOP dataset, this study pointed out that, at these latitudes, the diel variability at basin scale could be characterized only by increasing the spatio-temporal coverage of spaceborne lidar missions (e.g. reducing the distance between ground tracks). In fact, the observed CALIOP day/night variability is mainly driven by the spatial sampling differences of CALIOP day and night footprints. As CALIOP instrument was designed for atmospheric applications and it is not optimized to acquire the signal emerging from the water column, in our study only clear sky conditions were considered halving the available data profiles. Overall, only 5% of the CALIOP dataset fulfilled all the criteria in the retrieval filtering procedure and was successively analyzed.

Given the high correlation coefficient (R) between γ and δ_T for both Black Sea ($R = 0.91$) and Mediterranean ($R = 0.86$) datasets, already shown by Lu et al. (2014) at a global scale, δ_T was used as the focus parameter for this study, instead of an intermediate quantity for the derivation of standard ocean colour variables (e.g. b_{bp}, Chl-a). Thus, we analyzed the b_{bp} vs δ_T and Chl-a vs δ_T relationships:

- at a basin scale, δ_T and Chl-a are not correlated ($R = 0.42$ and $R = 0.1$ for MED and BS, respectively);
- δ_T and b_{bp} are correlated for waters characterized by $b_{bp} > 0.0015\ m^{-1}$, in both basins. This is more evident for the productive and optically complex waters of BS ($R = 0.84$) than for MED ($R = 0.61$) characterized by different trophic regimes.
- at sub-basin scale in MED, b_{bp} and δ_T are significantly correlated in bioregions and seasons characterized by high mean b_{bp} values (i.e. $b_{bp} > 0.0015\ m^{-1}$), whereas low R values correspond to summer, autumn and the oligotrophic bioregions.

Furthermore, the results of the δ_T vs Chl-a and δ_T vs b_{bp} annual cycle comparisons both at basins and sub-basin scales indicate a sort of '*dual*' behavior of the δ_T parameter: in the Black Sea, δ_T has a semi-annual cycle in very good agreement with b_{bp}; in the Mediterranean, δ_T shows also some similarities with Chl-a annual cycle.

The combined analysis of the b_{bp}:Chl-a, δ_T:Chl-a and δ_T:b_{bp} ratios in the Mediterranean bioregions stressed out the accordance between b_{bp}:Chl-a, and δ_T:Chl-a annual cycles with a west-to-east trophic gradient, similar to the results by Barbieux et al. (2018). The patterns observed through the δ_T:b_{bp} annual cycles pointed the potential

information of the δ_T parameter: here we hypothesize the lowering of δ_T:b_{bp} values from spring to summer to be related to changes in the phytoplankton community composition, which reflects the non-sphericity and the size of particles. This assumption is in agreement with the PSC seasonal variability in terms of particle density and volume concentration estimated by Di Cicco (2014) for MED oligotrophic bioregions (IO and LV).

In this study, CALIOP δ_T was used as an oceanic variable to describe the seasonal distributions of ocean particulate optical properties, providing information about the size and composition of ocean particles further than the estimates of Chl-a and POC concentrations. The results presented here confirm those obtained by a shipboard lidar by Collister et al. (2018), thus opening a new application for the use of CALIOP observations. A future challenge will be to characterize δ_T and b_{bp} also in terms of their differences as they could provide information about phytoplankton community composition. To enable quantitative comprehension of the information on the non-sphericity and size of ocean particles and hence on phytoplankton community composition from δ_T, two approaches need to be developed and combined: 1) theoretical models simulating lidar signal interaction with marine particles that take into account the different scattering effects (e.g. multiple scattering contribution); 2) experimental comparisons between in-situ inherent optical properties (IOPs) and polarization lidar measurements. In this work, we used the MED and BS as test-beds so that the natural follow-on will be to expand this approach to other regions (e.g. open ocean areas) or globally combining the standard ocean colour parameters with the added information brought by δ_T parameter.

Description of author's responsibilities

The conceptualization of this work was developed by DD, VEB, RS. Resources and funding acquisition for this work were provided by RS, VEB, SC, GV and DD. DD implemented the methodology and refined the data curation and the software of CALIOP retrieval procedure for ocean. DD performed most of the investigation and formal analysis with contributions and supervision of all co-authors. VEB, SC, GV, and RS contributed to the interpretation, the validation and the visualization of the results. DD wrote the original draft with input from all other co-authors. All co-authors provided the review and the editing of the manuscript.

Declaration of Competing Interest

The authors declare that they have no known competing financial interests or personal relationships that could have appeared to influence the work reported in this paper.

Acknowledgements

The NASA Langley Research Center is acknowledged for providing CALIOP version 4.1 Level 1 data through the Atmospheric Science Data Center (https://eosweb.larc.nasa.gov/HORDERBIN/HTML_Start.cgi). This work has been performed in the context of the Ocean Colour Thematic Assembly Centre of the Copernicus Marine Environment and Monitoring Service (grant number: 77-CMEMS-TAC-OC). Dr. Marco Bellacicco, Dr. Marco Bracaglia, Dr. Michela Sammartino and Dr. A. Di Cicco provided useful comments on earlier versions of this work. We acknowledge Dr. Michael Behrenfeld, Dr. James Campbell, Dr. Richard Gould, Dr. Johnathan Hair, Dr. Chris Hostetler, Dr. Yongxiang Hu, Dr. Ana Rice and Dr. Amy Jo Scarino for the useful discussion on the methodology implemented in this work. We acknowledge Dr. L. Caporaso for providing the ERA5 wind re-analysis.

References

Babichenko, S., Poryvkina, L., Rebane, O., Sobolev, I., 2016. Compact HLIF LiDAR for marine applications. Int. J. Remote Sens. 37, 3924–3937. https://doi.org/10.1080/01431161.2016.1204479.

Balch, W.M., Drapeau, D.T., Fritz, J.J., Bowler, B.C., Nolan, J., 2001. Optical backscattering in the Arabian Sea—continuous underway measurements of particulate inorganic and organic carbon. Deep-Sea Res. I Oceanogr. Res. Pap. 48 (11), 2423–2452. https://doi.org/10.1016/S0967-0637(01)00025-5.

Barbieux, M., Uitz, J., Bricaud, A., Organelli, E., Poteau, A., Schmechtig, C., et al., 2018. Assessing the variability in the relationship between the particulate backscattering coefficient and the chlorophyll a concentration from a global Biogeochemical-Argo database. J. Geophys. Res. Oceans 123, 1229–1250. https://doi.org/10.1002/2017JC013030.

Barbini, R., Colao, F., Fantoni, R., Palucci, A., Ribezzo, S., 1999. Shipborne laser remote sensing of the Venice lagoon. Int. J. Remote Sens. 20, 2405–2421. https://doi.org/10.1080/014311699212092.

Basterretxea, G., Font-Muñoz, J.S., Salgado-Hernanz, P.M., Arrieta, J., Hernández-Carrasco, I., 2018. Patterns of chlorophyll interannual variability in Mediterraneanbiogeographical regions. Remote Sens. Environ. 215, 7–17. https://doi.org/10.1016/j.rse.2018.05.027.

Behrenfeld, M.J., Halsey, H.K., Milligan, A.J., 2008. Evolved physiological responses of phytoplankton to their integrated growth environment. Philos. Trans. R. Soc. B 363, 2687–2703.

Behrenfeld, M.J., Hu, Y., Hostetler, C.A., Dall'Olmo, G., Rodier, S.D., Hair, J.W., et al., 2013. Space-based lidar measurements of global ocean carbon stocks. Geophys. Res. Lett. 40https://doi.org/10.1002/grl.50816. 4355–1120 4360.

Behrenfeld, M.J., Hu, Y., O'Malley, R.T., Boss, E.S., Hostetler, C.A., Siegel, D.A., et al., 2017. Annual boom–bust cycles of polar phytoplankton biomass revealed by space-based lidar. Nat. Geosci. 10, 118–122. https://doi.org/10.1038/ngeo2861.

Behrenfeld, M.J., Gaube, P., Della Penna, A., et al., 2019. Global satellite-observed daily vertical migrations of ocean animals. Nat. 576, 257–261. https://doi.org/10.1038/s41586-019-1796-9.

Bellacicco, M., Volpe, G., Colella, S., Pitarch, J., Santoleri, R., 2016. Role of photo-acclimation on phytoplankton's seasonal cycle in the Mediterranean Sea through satellite ocean color data. Remote Sens. Environ. 184, 595–604. https://doi.org/10.1016/j.rse.2016.08.004.

Bissonnette, L.R., 2005. Lidar and Multiple Scattering. Springer, Lidar, pp. 43–103.

Blondeau-Patissier, D., 2014. J. Gower, A.G. Dekker, S. Phinn, and V.E. Brando, 2014. A review of ocean color remote sensing methods and statistical techniques for the detection, mapping and analysis of phytoplankton blooms in coastal and open oceans. Prog. Oceanogr. 123, 123–144.

Brando, V.E., Braga, F., Zaggia, L., Giardino, C., Bresciani, M., Matta, E., Bellafiore, D., Ferrarin, C., Maicu, F., Benetazzo, A., Bonaldo, D., Falcieri, F.M., Coluccelli, A., Russo, A., Carniel, 2015. S.: High-resolution satellite turbidity and sea surface temperature observations of river plume interactions during a significant flood event. Ocean Sci. 11, 909–920. https://doi.org/10.5194/os-11-909-2015.

Brewin, R.J.W., Ciavatta, S., Sathyendranath, S., Jackson, T., Tilstone, G.H., Curran, K., Airs, R.L., Cummings, D.G., Brotas, V., Organelli, E., Dall'Olmo, G.D., Raitsos, D.E., 2017. Uncertainty in ocean-colour estimates of chlorophyll for phytoplankton groups. Front. Mar. Sci. 4 (104). https://doi.org/10.3389/fmars.2017.00104.

Bukin, O.A., Major, A., Yu, Pavlov, N., A., Shevtsov, B.M., Kholodkevich, E.D., 2001. Measurement of the lightscattering layers structure and detection of the dynamic processes in the upper ocean layer by shipborne layer. Int. J. Remote Sens. 19, 707–715. https://doi.org/10.1080/014311698215946.

Cai, C., Liou, K.N., 1982. Polarized light scattering by hexagonal icecrystals: theory. Appl. Opt. 21 (19), 3569–3580.

Cetinić, I., Perry, M.J., Briggs, N.T., Kallin, E., D'Asaro, E.A., Lee, C.M., 2012. Particulate organic carbon and inherent optical properties during 2008 North Atlantic Bloom Experiment. J. Geophys. Res. 117 (C6). https://doi.org/10.1029/2011JC007771.

Cho, B.C., Azam, F., 1990. Biogeochemical significance of bacterial biomass in the ocean ' s euphotic zone. Mar. Ecol. Ser. 63, 253–259.

Churnside, J.H., 2008. Polarization effects on oceanographic lidar. Opt. Express 16, 1196–1207. https://doi.org/10.1364/OE.16.001196.

Churnside, J.H., 2014. Review of profiling oceanographic lidar. Opt. Eng. 53 (5), 051405.

Churnside, J.H., Thorne, R.E., 2005. Comparison of airborne lidar measurements with 420 kHz echo-sounder measuremens of zooplankton. Appl. Opt. 44, 5504–5511. https://doi.org/10.1364/AO.44.005504.

Churnside, J.H., McCarty, B.J., Lu, X., 2013. Subsurface ocean signals from an orbiting polarization lidar. Remote Sens. 5, 3457–3475. https://doi.org/10.3390/rs5073457.

Churnside, J.H., Marchbanks, R., Lembke, C., Beckler, J., 2017. Optical backscattering measured by airborne lidar and underwater glider. Remote Sens. 9, 379. https://doi.org/10.3390/rs9040379.

Churnside, J., Hair, J., Hostetler, C., Scarino, A., 2018. Ocean backscatter profiling using high-spectral-resolution lidar and a perturbation retrieval. Remote Sens. 10, 2003. https://doi.org/10.3390/rs11151826.

Collister, B.L., Zimmermann, R.Z., Sukenik, C.I., Hill, V.J., Balch, W.M., 2018. Remote sensing of optical characteristics and particle distribution of the upper ocean using shipboard lidar. Remote Sens. Environ. 215, 85–96. https://doi.org/10.1016/j.rse.2018.05.032.

Cullen, J.J., 1982. The deep chlorophyll maximum: comparing vertical profiles of chlorophyll a. Can. J. Fish. Aquat. Sci. 39 (5), 791–803.

D'Alimonte, D., Zibordi, G., 2003. Phytoplankton determination in an optically complex coastal region using a multilayer perceptron neural network. IEEE T. Geosci. Rem. 41, 2861–2868. https://doi.org/10.1109/TGRS.2003.817682.

Dall'Olmo, G., Mork, K.A., 2014. Carbon export by small particles in the Norwegian Sea. Geophys. Res. Lett. 41 (8), 2921–2927. https://doi.org/10.1002/2014GL059244.

Di Cicco, A., 2014. Spatial and temporal variability of dominant Phytoplankton Size Classes in the Mediterranean Sea from Remote Sensing. In: PhD Thesis in Ecology and Management of Biological Resources, Tuscia University, pp. 1–110.

Di Cicco, A., Sammartino, M., Marullo, S., Santoleri, R., 2017. Regional empirical algorithms for an improved identification of phytoplankton functional types and size classes in the Mediterranean Sea using satellite data. Front. Mar. Sci. 4, 126. https://doi.org/10.3389/fmars.2017.00126.

D'Ortenzio, F., Ribera d'Alcalà, M., 2009. On the trophic regimes of the Mediterranean Sea: a satellite analysis. Biogeosciences 6, 139–148. https://doi.org/10.5194/bg-6-139-2009.

Gasol, Del Giorgio, Duarte, 1997. Biomass distribution in marine planktonic communities. Limnol. Oceanogr. 42, 1353–1363.

Getzewich, B.J., Vaughan, M.A., Hunt, W.H., Avery, M.A., Powell, K.A., Tackett, J.L., Winker, D.M., Kar, J., Lee, K.-P., Toth, T.D., 2018. CALIPSO lidar calibration at 532 nm: version 4 daytime algorithm. Atmos. Meas. Tech. 11, 6309–6326. https://doi.org/10.5194/amt-11-6309-2018.

Gordon, H.R., 1982. Interpretation of airborne oceanic lidar: effects of multiple scattering. Appl. Opt. 21, 2996–3001. https://doi.org/10.1364/AO.21.002996.

Harding Jr., L.W., Prezelin, B.B., Sweeney, B.M., Cox, J.L., 1981. Diel oscillations in the photosynthesis-irradiance relationship of a planktonic marine diatom. J. Phycol. 17, 389–394.

Harding Jr., L.W., Prezelin, B.B., Sweeney, B.M., Cox, J.L., 1982. Diel oscillations of the photosynthesis-irradiance (P-I) relationship in natural assemblages of phytoplankton. Mar. Biol. 67, 138–167.

Hersbach, H., 2016. The ERA5 Atmospheric Reanalysis. AGU Fall Meeting Abstracts.

Hostetler, C.A., Behrenfeld, M.J., Hu, Y., Hair, J.W., Schulien, J.A., 2018. Spaceborne lidar in the study of marine systems. Annu. Rev. Mar. Sci. 10, 121–147. https://doi.org/10.1146/annurev-marine-121916-063335.

Hu, Y., Powell, K., Vaughan, M., Tepte, C., Weimer, C., Beherenfeld, M., Young, S., Winker, D., Hostetler, C., Hunt, W., Kuehn, R., Flittner, D., Cisewski, M., Gibson, G., Lin, B., MacDonnell, D., 2007. Elevation information in tail (EIT) technique for lidar altimetry, opt. Express 15, 14504–14515. https://doi.org/10.1364/OE.15.014504.

Huang, J.P., Liu, J.J., Chen, B., Nasiri, S.L., 2015. Detection of anthropogenic dust using CALIPSO lidar measurements. Atmos. Chem. Phys. 15, 11653–11665. https://doi.org/10.5194/acp-15-11653-2015.

Jackson, T., Sathyendranath, S., Mélin, F., 2017. An improved optical classification scheme for the ocean colour essential climate variable and its applications. Remote Sens. Environ. https://doi.org/10.1016/j.rse.2017.03.036.

Jamet, C., Ibrahim, A., Ahmad, Z., Angelini, F., et al., 2019. Going beyond standard ocean color observations: lidar and polarimetry. Front. Mar. Sci. 2019. https://doi.org/10.3389/fmars.2019.00251.

Josset, D., Zhai, P.-W., Hu, Y., Pelon, J., Lucker, P.L., 2010a. Lidar equation for ocean surface and subsurface. Opt. Express 18, 20862–20875. https://doi.org/10.1364/OE.18.020862.

Josset, D., Pelon, J., Hu, Y., 2010b. Multi-instrument calibration method based on a multiwavelength ocean surface model. IEEE Geosci. Remote S. 7, 195–199. https://doi.org/10.1109/LGRS.2009.2030906.

Kajiyama, T., D'Alimonte, D., Zibordi, G., 2019. Algorithms merging for the determination of Chlorophyll-a concentration in the Black Sea. IEEE Geosci. Remote Sens. Lett. 6 (15), 677–681. https://doi.org/10.1109/LGRS.2018.2883539.

Kostadinov, T.S., Siegel, D.A., Maritorena, S., 2009. Retrieval of the particle size distribution from satellite ocean color observations. J. Geophys. Res. 114, C09015.

Le Traon, P.Y., Reppucci, A., Alvarez Fanjul, E., Aouf, L., Behrens, A., Belmonte, M., et al., 2019. From observation to information and users: The Copernicus Marine service perspective. Front. Mar. Sci. 6. https://doi.org/10.3389/fmars.2019.00234.

Lee, Z.P., Carder, K.L., Arnone, R.A., 2002. Deriving inherent optical properties from water color: A multi- band quasi-analytical algorithm for optically deep waters. Appl. Opt. 41, 5755–5772.

Li, J., Hu, Y., Huang, J., Stamnes, K., Yi, Y., Stamnes, S., 2011. A new method for retrieval of the extinction coefficient of water clouds byusing the tail of the CALIOP signal. Atmos. Chem. Phys. 11, 2903–2916. https://doi.org/10.5194/acp-11-2903-2011.

Liu, Z., Vaughan, M.A., Winker, D.M., Kittaka, C., Getzewich, B.J., Kuehn, R.E., Omar, A., Powell, K., Trepte, C., Hostetler, C.A., 2009. The CALIPSO lidar cloud and aerosol discrimination: version 2 algorithm and initial assessment of performance. J. Atmos. Ocean. Technol. 26, 1198–1213. https://doi.org/10.1175/2009JTECHA1229.1.

Lu, X., Hu, Y., Liu, Z., Zeng, S., Trepte, C., 2013. CALIOP receiver transient response study. Proc. SPIE 8873, 316–319. https://doi.org/10.1117/12.2033589.

Lu, X., Hu, Y., Trepte, C., Zeng, S., Churnside, J.H., 2014. Ocean subsurface studies with the CALIPSO spaceborne lidar. J. Geophys. Res. 119, 4305–4317. https://doi.org/10.1002/2014JC009970.

Lu, X., Hu, Y., Pelon, J., Trepte, C., Liu, K., Rodier, S., Zeng, S., Lucker, P., Verhappen, R., Wilson, J., Audouy, C., Ferrier, C., Haouchine, S., Hunt, B., Getzewich, B., 2016. Retrieval of ocean subsurface particulate backscattering coefficient from space-borne CALIOP lidar measurements. Opt. Express 24 (25), 29001–29008.

Lu, X., Hu, Y., Yang, Y., Vaughan, M., Liu, Z., Rodier, S., Hunt, W., Powell, K., Lucker, P., Trepte, C., 2018. Laser pulse bidirectional reflectance from CALIPSO mission. Atmos. Meas. Tech. 11, 3281–3296. https://doi.org/10.5194/amt-11-3281-2018.

Ludwig, W., Dumont, E., Meybeck, M., Heussner, S., 2009. River discharges of water and nutrients to the Mediterranean and Black Sea: Major drivers for ecosystem changes during past and future decades? Prog. Oceanogr. 80 (3–4), 199–217. https://doi.org/10.1016/j.pocean.2009.02.001.

Marty, J.C., Chiaverini, J., 2010. Hydrological changes in the Ligurian Sea (NW Mediterranean, DYFAMED site) during 1995–2007 and biogeochemical consequences. Biogeosciences 7 (7), 2117–2128. https://doi.org/10.5194/bg-7-2117-2010.

Mayot, N., D'Ortenzio, F., D'Alcal, A., R., M., Lavigne, H., Claustre, H., 2016. Interannual variability of the Mediterranean trophic regimes from ocean color satellites. Biogeosciences 13 (6), 1901–1917. https://doi.org/10.5194/bg-13-1901-2016.

McClain, C.R., 2009. A decade of satellite ocean color observations. Annu. Rev. Mar. Sci. 1, 9–42. https://doi.org/10.1146/annurev.marine.010908.163650.

McGill, M.J., Vaughan, M.A., Trepte, C.R., Hart, W.D., Hlavka, D.L., Winker, D.M., Kuehn, R., 2007. Airborne validation of spatial properties measured by the CALIPSO lidar. J. Geophys. Res. 112, D20201. https://doi.org/10.1029/2007JD008768.

Mishchenko, M.I., Hovenier, J.W., 1995. Depolarization of light backscattering by randomly oriented nonspherical particles. Opt. Lett. 20, 1356–1358. https://doi.org/10.1364/OL.20.001356.

Organelli, E., Claustre, H., Bricaud, A., Barbieux, M., Uitz, J., D'Ortenzio, F., Dall'Olmo, G.D., 2017. Bio-optical anomalies in the world's oceans: an investigation on the diffuse attenuation coefficients for downward irradiance derived from Biogeochemical Argo float measurements. J. Geophys. Res. Oceans 122, 3543–3564. https://doi.org/10.1002/2016JC012629.

Organelli, E., Dall'Olmo, G., Brewin, R.J., Tarran, G.A., Boss, E., Bricaud, A., 2018. The open-ocean missing backscattering is in the structural complexity of particles. Nat. Commun. 9 (1), 5439.

Qun, L., Xiaoyu, C., Weibiao, C., Chong, L., Jian, B., Yupeng, Z., Yudi, Z., Zhipeng, L., Peituo, X., Haochi, C., Dong, L., 2019. A semianalytic Monte Carlo radiative transfer model for polarized oceanic lidar: experiment-based comparisons and multiple scattering effects analyses. J. Quant. Spectrosc. Radiat. Transf. 237 (2019), 106638. ISSN 0022-4073. https://doi.org/10.1016/j.jqsrt.2019.106638.

Reuter, R., Willkomm, R., Krause, G., Ohm, K., 1995. Development of a shipboard lidar: technical layout and first results. EARSeL Adv. Remote Sens. 3, 15–25.

Sammartino, M., Di Cicco, A., Marullo, S., Santoleri, R., 2015. Spatio-temporal variability of micro-, nano- and pico-phytoplankton in the Mediterranean Sea from satellite ocean colour data of SeaWiFS. Ocean Sci. 11 (5), 759–778. https://doi.org/10.5194/os-11-759-2015.

Sassen, K., 1991. The polarization lidar technique for cloud research: A review and current assessment. Bull. Am. Meteorol. Soc. 71, 1848–1866.

Sassen, K., 2005. Polarization in lidar. In: Weitkamp, C. (Ed.), LIDAR—Range-Resolved Optical Remote Sensing of the Atmosphere. Springer, New York, pp. 19–42.

Sathyendranath, S., Brewin, R.J., Brockmann, C., Brotas, V., Calton, B., Chuprin, A., Cipollini, P., Couto, A.B., Dingle, J., Doerffer, R., Donlon, C., Dowell, M., Farman, A., Grant, M., Groom, S., Horseman, A., Jackson, T., Krasemann, H., Lavender, S., Martinez-Vicente, V., Mazeran, C., Mélin, F., Moore, T.S., Müller, D., Regner, P., Roy, S., Steele, C.J., Steinmetz, F., Swinton, J., Taberner, M., Thompson, A., Valente, A., Zühlke, M., Brando, V.E., Feng, H., Feldman, G., Franz, B.A., Frouin, R., Gould Jr., R.W., Hooker, S.B., Kahru, M., Kratzer, S., Mitchell, B.G., Muller-Karger, F.E., Sosik, H.M., Voss, K.J., Werdell, J., Platt, T., 2019. An ocean-colour time series for use in climate studies: the experience of the ocean-colour climate change initiative (OC-CCI). Sensors 19, 4285. https://doi.org/10.3390/s19194285.

Schulien, J.A., Behrenfeld, M.J., Hair, J.W., Hostetler, C.A., Twardowski, M.S., 2017. Vertically-resolved phytoplankton carbon and net primary production from a high spectral resolution lidar. Opt. Express 25, 13577–13587. https://doi.org/10.1364/OE.25.013577.

Siegel, D.A., Behrenfeld, M.J., Maritorena, S., McClain, C.R., Antoine, D., Bailey, S.W., Yoder, J.A., 2013. Regional to global assessments of phytoplankton dynamics from the SeaWiFS mission. Remote Sens. Environ. 135, 77–91. https://doi.org/10.1016/j.rse.2013.03.025.

Siokou-Frangou, I., Christaki, U., Mazzocchi, M.G., Montresor, M., Ribera D'Alcal_a, M., Vaqu_e, D., and Zingone, A., 2010. Plankton in the open Mediterranean Sea: a review. Biogeosciences 7 (5), 1543–1586. https://doi.org/10.5194/bg-7-1543-2010.

Stramski, D., Reynolds, R.A., Kahru, M., Mitchell, B.G., 1999. Estimation of particulate organic carbon in the ocean from satellite remote sensing. Science 285 (5425), 239–242.

Stramski, D., Boss, E., Bogucki, D., Voss, K.J., 2004. The role of seawater constituents in light backscattering in the ocean. Prog. Oceanogr. 61 (1), 27–56.

Takano, Y., Liou, K.N., 1989. Solar radiative transfer in cirrus clouds. part 1: Single-scattering and optical properties of hexagonal ice crystals. J. Atmos. Sci. 46, 3–18.

Volpe, G., Santoleri, R., Vellucci, V., Ribera d'Alcala, M., Marullo, S., D'Ortenzio, F., 2007. The colour of the Mediterranean Sea: global versus regional bio-optical algorithms evaluation and implication for satellite chlorophyll estimates. Remote Sens. Environ. 107, 625–638.

Volpe, G., Colella, S., Brando, V.E., Forneris, V., La Padula, F., Di Cicco, A., Sammartino, M., Bracaglia, M., Artuso, F., Santoleri, R., 2019. Mediterranean ocean colour Level 3 operational multi-sensor processing. Ocean Sci. 15, 127–146. https://doi.org/10.5194/os-15-127-2019.

Winker, D.M., Vaughan, M.A., Omar, A., Hu, Y., Powell, K.A., Liu, Z., Hunt, W.H., Young, S.A., 2009. Overview of the CALIPSO mission and CALIOP data processing algorithms. J. Atmos. Ocean. Technol. 26, 2310–2323. https://doi.org/10.1175/2009jtecha1281.1.

Xing, X., Qiu, G., Boss, E., Wang, H., 2019. Temporal and vertical variations of particulate and dissolved optical properties in the South China Sea. J. Geophys. Res. Oceans 124, 3779–3795. https://doi.org/10.1029/2018JC014880.

Yang, P., Liou, K.N., 1996. Geometrics-optics-integral-equation method for light scattering by non-spherical ice crystals. Appl. Opt. 35, 6568–6584.

Zibordi, G., Mélin, F., Berthon, J.-F., Talone, M., 2015. In situ autonomous optical radiometry measurements for satellite ocean color validation in the western black sea. Ocean Sci. 11 (2), 275–286. https://www.ocean-sci.net/11/275/2015/.